Int. J. Heat Mass Transfer. Vol. 36, No. 4, pp. 1007–1018, 1993
Printed in Great Britain

0017-9310/93 $6.00 + 0.00

Thermophoretic transport in the outside vapor deposition process

S. H. KANG† and R. GREIF
Department of Mechanical Engineering, University of California at Berkeley, Berkeley, CA 94720, U.S.A.

(*Received* 4 *September* 1991 *and in final form* 9 *March* 1992)

Abstract—A study has been made of the flow, heat transfer and thermophoretic deposition to a circular boule in respect to the outside vapor deposition (OVD) process. Numerical solutions of the governing conservation equations have been obtained utilizing a non-orthogonal curvilinear coordinate grid. The particle deposition rate and the variation of the deposition efficiency are investigated for a range of parameters relative to the OVD process. The interaction of the jet-like torch flow with the target and the surroundings results in a flow, heat transfer and particle transport to the circular target that are quite different from that for uniform flow. The increase in the concentration prior to the target is an important factor in determining the particle deposition rate. The effects of buoyancy augment the deposition rate. Larger values of the average Nusselt number and the efficiency are obtained for a cold target. For a hot target, the local Nusselt number becomes negative over the leeward side and a particle-free layer is formed. For the particle jet, the concentration and the deposition rate rapidly decrease downstream from the stagnation point. The deposition efficiency is greatly reduced when the torch is not aligned with respect to the target. Increasing the speed of the gas flow increases the average Nusselt number, but reduces the efficiency. Higher efficiency is obtained for a higher torch temperature. The efficiency is slightly increased for a larger target. Increasing the distance between the torch and the target and increasing the rotational speed of the boule slightly reduce the efficiency.

1. INTRODUCTION

THE MANUFACTURE of high quality wave guides has been successfully carried out utilizing particle deposition techniques. In the outside vapor deposition (OVD) process, the torch is composed of concentric rings or linear slits through which $SiCl_4$, CH_4, O_2 and N_2 or He gases flow, and impinge on a cylindrical target. Silica particulates are formed by direct oxidation or hydrolysis reactions. Typically, the first particles formed are of the order of 0.1 μm in diameter and these grow by collision and coalescence to produce particles up to 0.25 μm (Morrow *et al.* [1], Bautista *et al.* [2]).

Homsy *et al.* [3] and Batchelor and Shen [4] analyzed the thermophoretic deposition of particles in a uniform flow past a cylinder based on the Blasius series solution. Gokoglu and Rosner [5, 6] analyzed the thermophoretic mass transfer on the cold flat plate. Garg and Jayaraj [7, 8] calculated thermophoretic deposition over a cylinder in numerical studies specifying the pressure gradient of the external flow. Alam *et al.* [9] investigated thermophoretic deposition for a plane jet impinging on a flat plate. These studies utilized the boundary layer assumptions with simple external flows. However, experimental results (Bautista *et al.* [10], Graham and Alam [11]) showed that the circumferential variation of the flow and heat transfer, as well as the interaction between the torch and the boule, have strong effects on the particle deposition. The utilization of electric fields to enhance and control particle deposition have been studied experimentally and theoretically by Hwang and Daily [12–14].

A study was made of a forced buoyant jet impinging on a circular cylinder by solving the governing elliptic conservation equations (Kang and Greif [15]) and results for the flows and heat transfer were presented for a constant property flow using the Boussinesq approximation. It is noted that the flow and temperature fields for a forced buoyant impinging jet are quite different from those present in a uniform flow. As the air leaves the nozzle, the jet is assumed to develop from a potential core region. Beyond the stagnation point the flow accelerates and develops into a wall jet which separates downstream. A recirculation bubble forms at the rear of the cylinder and further downstream a buoyant jet develops. The flow cools due to heat loss to the ambient and to heat transfer to the target boule. In the present study a high temperature variable property flow is considered with particles assumed to form at the exit from the torch. The particles are convected downstream by the flow and thermophoretic velocity. In this work, the particle deposition rate is determined and the variation of the deposition efficiency is investigated over a range of

† Visiting Professor from Seoul National University, Seoul 151-742, Korea.

NOMENCLATURE

A_i convection–diffusion coefficients
a^i contravariant base vector
b source term in the discretized equation
C concentration of the particles
C_f skin-friction coefficient, $2\tau_w/\rho_j U_j^2$
C_p pressure coefficient, $2/\rho_j U_j^2$
c_p specific heat at constant pressure
F mass flux of the particles
g square of the Jacobian
g_v acceleration of gravity
g^{ij} components of the contravariant metric tensor
H distance between the nozzle and the cylinder
i, j Cartesian base vectors
J deposition coefficient, $v_{th,w} C_w/U_j C_j$
K coefficient of the thermophoretic velocity
k conductivity
L_s separation length
N rotational speed of the target
Nu Nusselt number, $qR/k_j(T_j - T_a)$
Pr Prandtl number, $\mu c_p/k$
p static pressure
R radius of a cylinder
Re Reynolds number, $\rho_j U_j R/\mu_j$
S_ϕ source term in the governing equation
T temperature
U^i contravariant velocity component
U_j magnitude of the gas jet velocity
u, v Cartesian components of the velocity
W width of the jet
x, y Cartesian coordinate.

Greek symbols
Γ general diffusive coefficient
η deposition efficiency
Θ non-dimensional temperature, $(T_w - T_a)/(T_j - T_a)$
Θ^* non-dimensional parameter, $T_a/(T_j - T_a)$
θ angle measured from the front stagnation point
μ viscosity
ν kinematic viscosity
ξ^i curvilinear coordinate, $\xi^1 = \xi$, $\xi^2 = \eta$
ρ density
τ_w wall shear stress
ϕ general dependent variable
Ω rotational speed, $2\pi N/60$.

Subscripts
N, S, E, W four nodes around the grid point P
a ambient value
c values of particle jet
j values at the torch exit
o values at the stagnation point
w values at the target wall
ξ^i partial differentiation with respect to ξ^i.

values of the parameters. The flow is assumed to be laminar and steady throughout the entire domain, where a buoyancy force is acting vertically.

2. MATHEMATICAL MODELING

2.1. *Coordinates and governing equations*

The gas is assumed to be homogeneous and non-reactive with particles being formed at the exit of the torch. The governing steady, laminar conservation equations are described in the Cartesian coordinate system, where u and v denote velocity components in the x- and y-directions, respectively (cf. Fig. 1(a)). A non-orthogonal curvilinear coordinate grid is generated to carry out the numerical calculations [16–18]. The local heat transfer and the particle deposition on the surface of the boule, especially near the stagnation point, are of interest, and the so called C-type grid system is adopted [15, 16]. The center line of the wake ($x > 1.0$, $y = 0.0$) is a branch-cut which transforms the flow domain to a rectangular region as is shown in Fig. 1(b). Transformation functions $\xi(x, y)$ and $\eta(x, y)$ are obtained by solving Poisson equations [17, 18].

The continuity, x-momentum, y-momentum, and energy equations in an arbitrary curvilinear coordinate system are as follows:

$$(\sqrt{(g)}\rho U^i)_{\xi^i} = 0 \tag{1}$$

$$[\sqrt{g}(\rho U^i u - \mu g^{ij} u_{\xi^j})]_{\xi^i} + (y_{\xi^2} p)_{\xi^1} - (y_{\xi^1} p)_{\xi^2} - \sqrt{g} g_v (\rho - \rho_a) = 0 \tag{2}$$

$$[\sqrt{g}(\rho U^i v - \mu g^{ij} v_{\xi^j})]_{\xi^i} + (x_{\xi^2} p)_{\xi^1} - (x_{\xi^1} p)_{\xi^2} = 0 \tag{3}$$

$$[\sqrt{g}(\rho c_p U^i T - k g^{ij} T_{\xi^j})]_{\xi^i} = 0 \tag{4}$$

where

$$\xi^1 = \xi, \quad \xi^2 = \eta, \quad U^i = \bar{a}^i \cdot (u\hat{i} + v\hat{j})$$
$$\bar{a}^i = \nabla \xi^i, \quad g^{ij} = \bar{a}^i \cdot \bar{a}^j. \tag{5}$$

Since the flow is low-pressure and low-speed, the pressure work and dissipation terms are neglected in the energy equation. Density ρ, viscosity μ, specific heat at constant pressure c_p, and conductivity k are variable and given as functions of the temperature.

The gas is considered to be particle free because of the dilute particle concentration. The particle transport is affected by convection, diffusion, and thermophoresis. The contribution to the deposition rate due

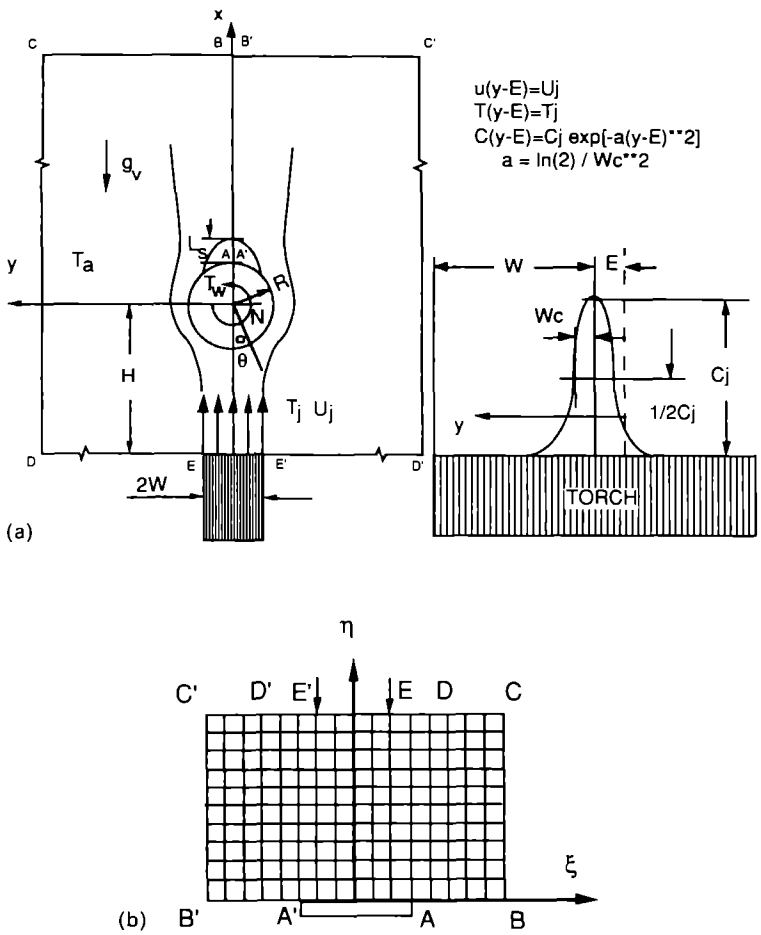

FIG. 1. (a) Flow configuration and coordinate system. (b) Transformed domain for numerical calculations.

to Brownian diffusion is normally much smaller than that due to thermophoresis and is neglected (Homsy *et al.* [3], Batchelor and Shen [4]). The conservation equation for the particle concentration is then given by:

$$[\sqrt{g}(U^i_{\mathrm{eff}}C)]_{,i} = 0 \tag{6}$$

where U^i_{eff} is the sum of the flow and the thermophoretic velocities. The thermophoretic velocity is given as

$$\vec{v}_{\mathrm{th}} = -K\frac{\nu}{T}\nabla T \tag{7}$$

where the thermophoretic coefficient K is a function of the Knudsen number and the ratio of the thermal conductivity of the gas to that of the particle (Talbot *et al.* [19]). A value of K equal to 0.9 is used (Walker *et al.* [20]). The effects of K on the values of the concentration and deposition efficiency at the stagnation point are discussed in Appendix B.

2.2. *Boundary conditions*

The no-slip condition for the velocity components and the condition of constant wall temperature are given on A′–A which is the transformed circular cylinder, i.e. $u = R\Omega \sin\theta$, $v = -R\Omega\cos\theta$, $T = T_w$. Neglecting diffusion in the concentration equation results in a hyperbolic equation and a boundary condition is not required on the wall. The velocities and temperature along B′–A′ are equal to the value along A–B. On E′–E, corresponding to the torch exit, the velocity and temperature are uniform, i.e. $u = U_j$, $v = 0$, and $T = T_j$. The static pressure is fixed to be zero here as a reference value. The particle concentration is given by the Gaussian normal distribution (Bautista *et al.* [10], Graham and Alam [11]):

$$C(y-E) = C_j \exp\left[-\ln 2\left(\frac{y-E}{W_c}\right)^2\right] \tag{8}$$

where E is the horizontal eccentricity of the torch relative to the center line. W_c denotes the half width of the particle jet so that at $y-E = W_c$, $C = C_j/2$. On the boundary C′–D′ and D–C, which is located far from the cylinder, the y-derivative of the entrained horizontal velocity component is taken to be zero: $\partial v/\partial y = 0$. The boundary condition for u is deter-

mined by considering the entrained flow to be irrotational: $\partial^2 u/\partial y^2 = 0$. The entrained flow is assumed to be horizontal at the external upstream boundary; D–E and E′–D′. This assumption does not have a strong effect on the flow pattern and heat transfer over the cylinder. The temperature on the external boundary is at the constant ambient value and the concentration is zero: $T = T_a$, $C = 0$. At the far downstream location above the cylinder B′–C′ and B–C, the streamwise second derivatives of the velocity components and the temperature are assumed to be zero. No boundary condition for concentration is required there.

2.3. *Deposition of particles and specified relations*

The deposition rate is equal to the normal component of the thermophoretic velocity multiplied by the particle concentration at the wall. The non-dimensional deposition coefficient, J is defined by

$$J = \frac{v_{th,w} C_w}{U_j C_j} = K \frac{1}{\Theta_w + \Theta^*} \left(\frac{\nu_w}{\nu_j}\right)\left(\frac{k_j}{k_w}\right)\left(\frac{C_w}{C_j}\right)\frac{Nu}{Re}. \quad (9)$$

When the heat-transfer rate is negative, the particle transport is away from the surface and a particle-free layer is formed near the wall. For this case, C_w and J are zero. In general, the concentration at the wall, C_w, is obtained by considering the boundary layer equations (cf. Appendix A). The deposition efficiency is defined as the ratio of the total deposition rate, F_w, to the incoming particle mass flow rate, F_{in}:

$$\eta = \frac{F_w}{F_{in}} = \frac{F_w}{\int_{-\infty}^{\infty} U_j C_{in}\, dy} = 2\sqrt{(\pi \cdot \ln 2)}\left(\frac{R}{W_c}\right)\bar{J} \quad (10)$$

where

$$F_w = 2\pi R \bar{J} U_j C_j, \quad \bar{J} = \frac{1}{2\pi}\int_{-\pi}^{\pi} J\, d\theta.$$

3. NUMERICAL METHOD

The governing equations (1)–(4) and (6) can be written in a generalized form according to

$$[\sqrt{g}(\rho U^i \phi - \Gamma g^{ij}\phi_{\xi^j})]_{\xi^i} - b = 0 \quad (11)$$

where ϕ denotes an arbitrary variable. The discretized form of the equations is obtained by the finite volume method (cf. Patankar [21]), and is written as

$$A_P\phi_P = A_N\phi_N + A_S\phi_S + A_E\phi_E + A_W\phi_W + S_\phi. \quad (12)$$

The coefficients A_i are obtained by integrating the convective and diffusive fluxes across the control surfaces and the subscripts N, S, E, and W denote the four neighboring grid points around P. Since the Reynolds numbers are not large, the HYBRID scheme [21] is used. The quantity S_ϕ includes all the terms proportional to the control volume and non-orthogonal related terms.

The calculation of the pressure proceeds according to the SIMPLE algorithm of Patankar [21]. Linearized solutions of the momentum equation are used at each control surface to evaluate the fluxes. These are obtained by using the velocities and pressures at neighboring points [15, 17, 18].

A Modified Strongly Implicit (MSI) method (Schneider and Zedan [22]) is adopted to solve the discretized linear equations. The overall solution is iterative in nature and convergence is checked by monitoring the sum of the residuals for the variables over the entire domain. The equation for the particle concentration, which is linear and decoupled from the other equations, is solved after the flow and temperature fields are obtained. The program developed in the previous study [15] is modified to include variable properties and the concentration equation for the particles.

4. RESULTS AND DISCUSSION

4.1. *Scope of study and preliminary calculations*

The important quantities are the radius of the target boule R, the distance between the torch and the boule H, the half width of the torch W, the eccentricity of the torch relative to the boule E, the jet velocity U_j and temperature T_j, the surface temperature of the boule T_w, the half width of the particle jet W_c, and the rotational speed of the boule N. The values used are:

R = 0.0070, **0.0100**, 0.0143 (m)

U_j = 1.0, 1.5, **2.0** (m s^{-1})

T_j = 1600, 1800, **2000** (K)

$\Theta_w\ [=(T_w - T_a)/(T_j - T_a)]$ = 0.0–**0.5**–1.0

W/R = 0.7, **1.0**, 1.4

H/R = 3.5, **5.0**, 7.0

W_c/R = **0.05**, 0.10

E/W_c = **0.0**, 1.0, 2.0

N = **0**, 60, 120, 300 (r.p.m.).

The bold faced values are the standard values of each quantity when the others are changed. The ambient temperature T_a is fixed as 300 K.

The upstream and downstream locations were chosen to be $-H$ and $20.0R$, and the external boundaries were located at $\pm 10.0R$ [15]. The grids were non-uniformly and more closely spaced near the surface and in the wake of the cylinder. Three sets of grid points were tested for grid sensitivity; 111×41, 131×61, and 151×71 in the ξ and η directions, respectively. The solution is considered to be converged when the non-dimensionalized residuals become less than 10^{-5} for the concentration and 10^{-4} for the velocities and temperature. The results of calculations for the standard values given above are summarized

Table 1. Variation of calculated results for air for standard values of variables

Number of grids	111 × 41	131 × 61	151 × 71
Maximum $C_f Re^{1/2}$ (location)	3.680 (50.1°)	3.648 (44.2°)	3.642 (44.2°)
Separation point θ_s	126	128	129
Separation length L_s/R	1.66	1.61	1.59
Stagnation pressure coefficient C_{po}	1.90	2.03	2.04
Stagnation Nusselt number $Nu_0/Re^{1/2}$	0.356	0.357	0.357
Average Nusselt number	1.120	1.131	1.136
Stagnation deposition rate $J_0\ Re^{1/2}$	0.326	0.330	0.331
Deposition efficiency η	45.2	60.1	61.5

in Table 1 and 151 × 71 grids are chosen for the present study.

4.2. *Effects of buoyancy and the base gas*

Calculations were carried out with and without the buoyancy term. For most cases, air was chosen as the base gas although calculations were also made for helium. The density of helium is small, and the kinetic viscosity and thermal diffusivity are large in comparison with air. Calculations were carried out for the standard values of the variables. The overall flow patterns and isothermal contours show the same symmetric structure as for the constant property flow [15]. The Reynolds numbers based on the properties at the torch exit are 53.3 and 7.03, for air and helium, respectively. The variations of the velocity and the temperature along the center line of the jet are shown in Fig. 2. In the absence of buoyancy, the free jet from the torch diffuses, and the velocity along the center line decreases monotonically to zero at the stagnation point. Near the stagnation point, the flow spreads laterally and forms the wall jet layer over the surface of the target cylinder. The flow separates downstream and a recirculation bubble results. When buoyancy is present, the flow accelerates as it leaves the torch location and then decreases to zero as the cylinder is approached. The gas jet cools by lateral heat conduction and the temperature decreases to the wall temperature at the stagnation point. The acceleration resulting from buoyancy contributes to the increases of the skin-friction and the heat transfer coefficient.

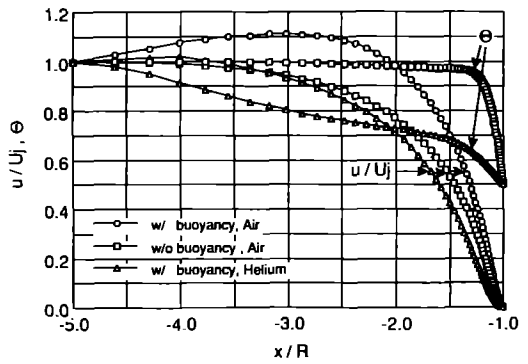

FIG. 2. Effect of buoyancy and base gas (He) on the variations of velocity and temperature along the center line of the torch flow.

These distributions, scaled by the square root of the Reynolds number, are shown in Figs. 3(a) and (b). The wall jet becomes thin and accelerates due to buoyancy (Fig. 4) where the wall jet profiles at $\theta = 90°$ are shown. With buoyancy present, the flow separates at 128°; without buoyancy separation occurs at 105°. The separation length, L_s/R, which is measured from the rear stagnation point decreases from 7.04 to 1.47 due to buoyancy. Buoyancy delays separation and makes the recirculation region smaller.

For helium as the base gas, the acceleration due to buoyancy is suppressed by the strong diffusion, and the jet cools rapidly due to the large heat conduction (Fig. 2). The wall jet therefore becomes thicker, the maximum velocity decreases and the temperature

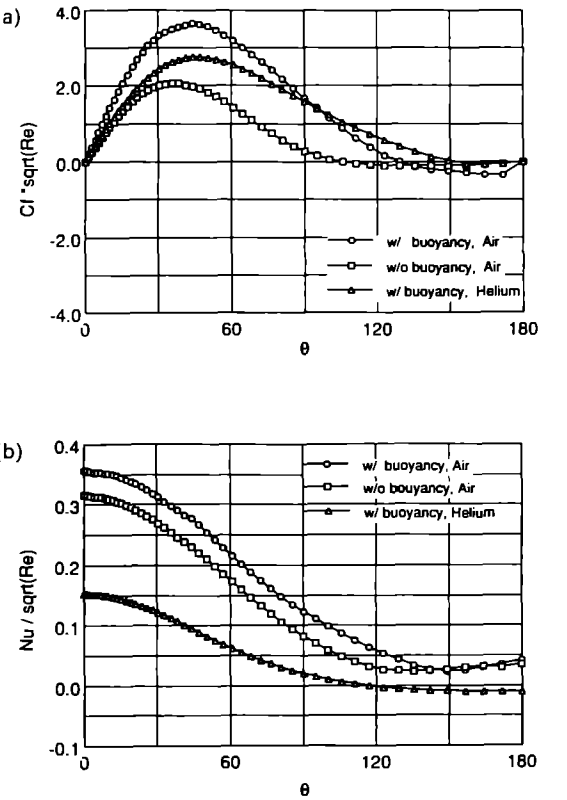

FIG. 3. (a) Effect of buoyancy and base gas (He) on the variations of skin-friction on the target surface. (b) Effect of buoyancy and base gas (He) on the distributions of Nusselt number on the target surface.

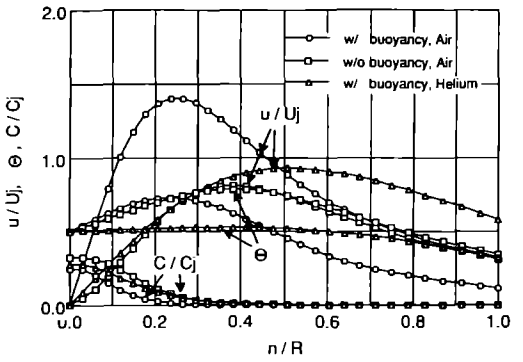

FIG. 4. Velocity, temperature and concentration profiles in the wall jet at $\theta = 90^\circ$.

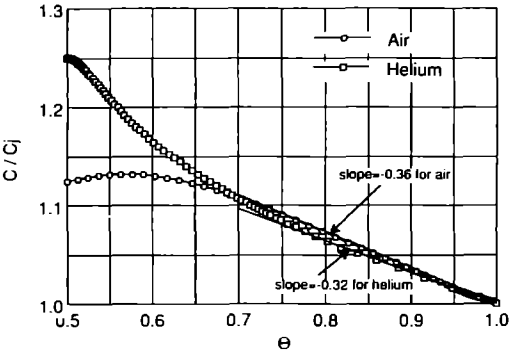

FIG. 6. Temperature–concentration plot along the center line of the torch.

cools to the wall temperature at $\theta = 90^\circ$ (Fig. 4). However, the small inertia (small density, $Re = 7.03$) delays the separation point until $\theta = 152^\circ$ and makes the recirculation bubble very small, $L_s/R = 0.54$. The value of Nusselt number becomes negative at $\theta = 119^\circ$ in Fig. 3(b), i.e. the flow cannot heat the target beyond this location.

The concentration increases moderately in the free jet region, but undergoes a rapid increase in the stagnation region (Fig. 5). The variations of the concentration and the temperature along the center line of the torch are related by (cf. Appendix B):

$$\frac{C}{C_j} = \left[\frac{\Theta+\Theta^*}{1.0+\Theta^*}\right]^{-m}. \tag{13}$$

When the non-dimensional concentration and temperature do not deviate greatly from 1.0, the values of m are 0.36 and 0.32 for air and helium, respectively as shown in Fig. 6. Note that the corresponding power, $(1.0-K^*\,Pr)$ in equation (B7) has values of 0.37 and 0.33 for air and helium, respectively.

The thermophoretic velocities on the wall, which are proportional to the Nusselt number (equation (9)), increase due to buoyancy (Fig. 7). Note that helium gas has a larger thermophoretic velocity at the stagnation point. The concentration and deposition coefficient distributions are shown in Figs. 8(a) and (b). The concentration decreases from the stagnation point to downstream locations, and becomes very small in the recirculation region (the entrained flow from outside has a low concentration). In the case of helium, the concentration is zero over the negative Nusselt number region, i.e. a particle-free layer is formed. The deposition rate over the flow separation region is very small. The deposition flux rapidly decreases from the stagnation point. Note that for the uniform flow case (Garg and Jayaraj [7, 8]) the concentration is nearly uniform and the deposition rate decreases parabolically along the circular cylinder. The deposition efficiencies for the three cases, i.e. with and without buoyancy for air, and with buoyancy for helium, are 61.4, 51.5, and 56.7%, respectively.

4.3. *Effects of the surface temperature and the width of the particle jet*

The thermophoretic velocity at the wall, which is proportional to the Nusselt number, is strongly dependent on the surface temperature. For a range of surface temperatures, the Nusselt number distributions are presented in Fig. 9. As the surface becomes hotter, the Nusselt number decreases, and becomes negative over a portion of the leeward side.

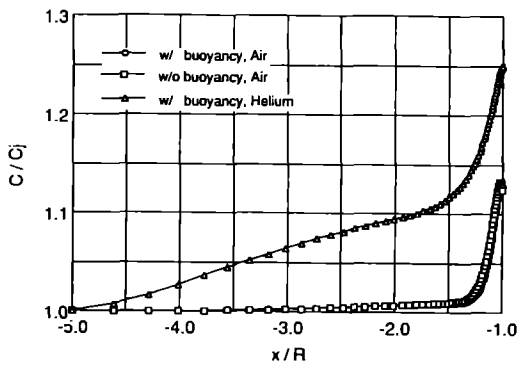

FIG. 5. Effect of buoyancy and base gas (He) on the variations of the center line concentration prior to the target.

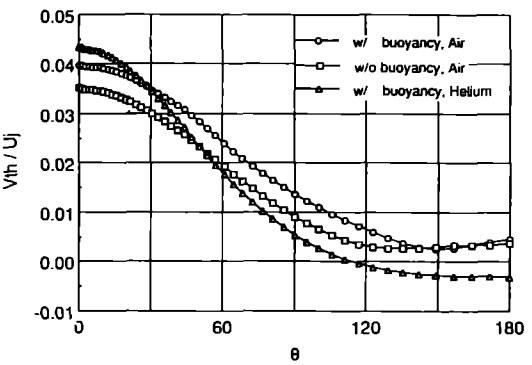

FIG. 7. Variations of the thermophoretic velocity due to buoyancy and the base gas, He.

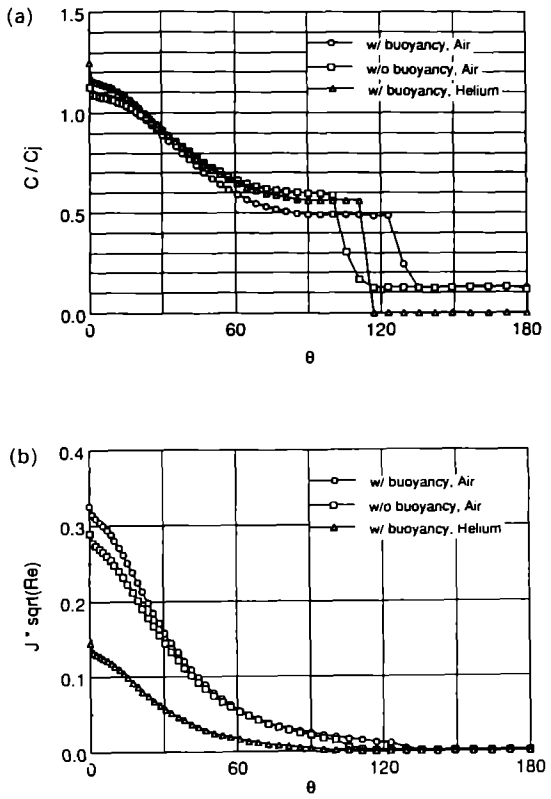

FIG. 8. (a) Effect of buoyancy and base gas (He) on the distributions of particle concentration on the target surface. (b) Effect of buoyancy and base gas (He) on the deposition rate coefficients on the target surface.

When the surface temperature is very hot, the Nusselt numbers are negative over the entire surface. For this condition the torch does not heat the target and the particle-free layer extends over the entire surface. The average Nusselt number decreases and is negative when the non-dimensional wall temperature, Θ_w, is larger than 0.89 (Fig. 10(a)). As the surface temperature becomes cold, the deposition rate becomes large near the stagnation point, but is not always large downstream, because the increased deposition rate upstream makes the concentration smaller downstream (not shown).

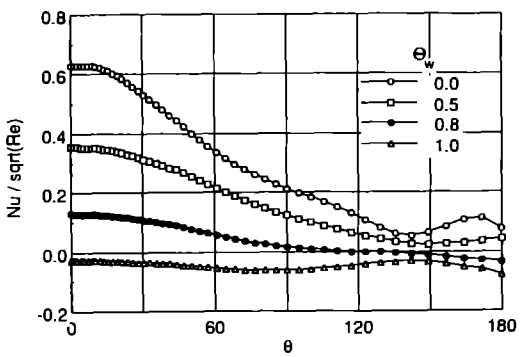

FIG. 9. Variations of the local Nusselt number on the surface with the surface temperature of the target.

As the particle jet becomes thin relative to the target and the gas jet, small W_c/R, the local concentration and the local deposition rate rapidly decrease from the stagnation point to downstream locations. However, the overall deposition and deposition efficiency increase for small W_c/R. The variation of the efficiency with respect to the width of the particle jet for different surface temperatures is presented in Fig. 11(a). If the surface is cold and the particle jet is thin, the particle deposition is large. The torch–target configuration and the operating target temperature are important parameters characterizing the process.

4.4. *Effects of the eccentricity of the torch*

The misalignment (eccentricity) of the torch with respect to the target destroys the symmetry of the flow and the particle jet. This misalignment (cf. Fig. 1(a)) is known to have a strong effect on deposition (Bautista *et al.* [10]) and is studied by introducing an eccentricity, E. Note that when E/W_c is 2.0, the misalignment E is $0.1R$ for $W_c/R = 0.05$. For this condition there is only a small change in the Nusselt number distribution (not shown); however, for the concentration and deposition the maximum values are reduced and the curves shift toward and past the center line of the torch (Figs. 12(a) and (b)). The large reduction of the deposition efficiency in Fig. 13 is primarily due to the large reduction in particle concentration prior to reaching the target. The values without the stars in Fig. 13 are the calculated efficiencies when only the particle jet is shifted (the torch being kept at the original position). Control of the particles is very important in respect to attaining high efficiency of the process.

4.5. *Effects of the velocity, temperature and width of the gas jet*

The velocity of the gas-mixture is an important operating parameter. The Reynolds numbers corresponding to the velocities of 1.0, 1.5 and 2.0 m s^{-1} are 26.7, 40.0 and 53.3, respectively. Over this range of values, as the velocity decreases, the effect of the flow acceleration by buoyancy become large; the gas jet is cooled significantly. The skin-friction coefficients decrease (not shown), and the local and the average Nusselt numbers (cf. Fig. 10(b)) increase for increased velocity. There is a slight reduction in the efficiency with increased velocity in Fig. 11(b).

For gas jet temperatures of 1600, 1800 and 2000 K, the Reynolds numbers are 77.4, 63.6 and 53.3, respectively. The distributions of the skin-friction coefficients, Nusselt numbers and deposition coefficients scaled by the square root of the Reynolds number are not noticeably changed with respect to jet temperature. The average Nusselt number is proportional to the square root of the Reynolds number and to the -0.88 power of the temperature (Fig. 10(c)). The higher jet temperature yields a higher

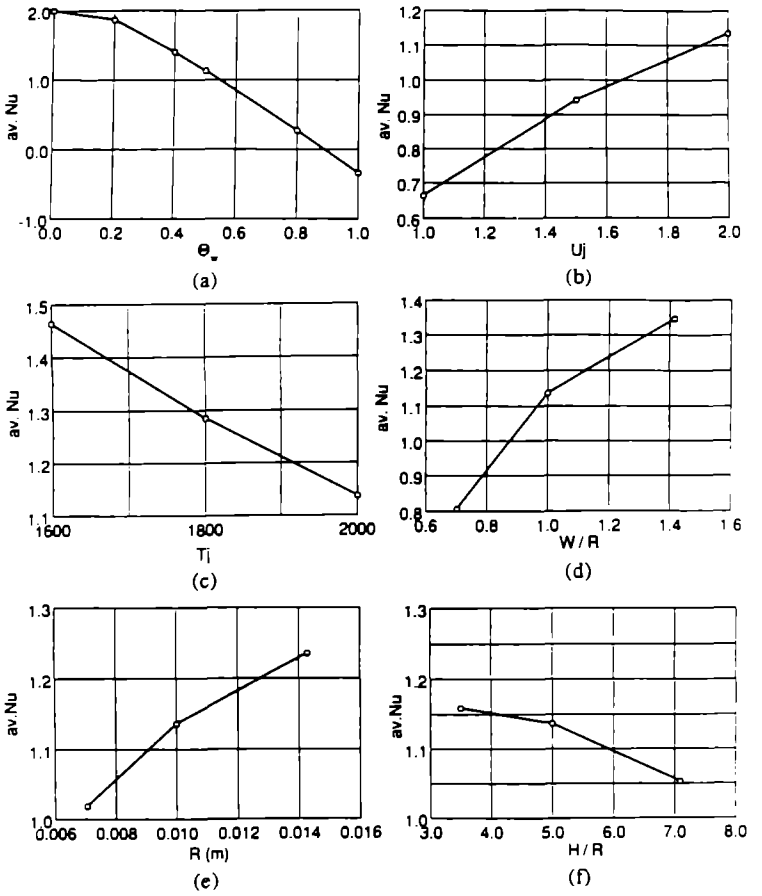

FIG. 10. Variations of the average Nusselt number with variables: (a) Θ_w and W_c/R; (b) U_j; (c) T_j; (d) W/R; (e) R; (f) H/R.

efficiency, proportional to the 0.88 power of the temperature (Fig. 11(c)).

The local Nusselt numbers and deposition coefficients increase over the target when the width of the gas jet is large (not shown). The increases in the average Nusselt numbers and the efficiencies with respect to the width W are shown in Figs. 10(d) and 11(d).

4.6. *Effects of the radius of the target and the position of the torch*

For a larger target, the distance between the torch exit and the target is shorter and the blockage effect of the target on the flow is increased. The average Nusselt number increases with increasing values of the radius (Fig. 10(e)). The deposition rate at a given angular location is smaller for the larger target. The cumulative deposition along the target from the stagnation point to a given location is larger for a larger target (Fig. 14(a)); however, the total deposition rate, i.e. the efficiency, is only slightly increased as shown in Fig. 11(e).

For the condition when the distance between the torch and the target increases, the average Nusselt number decreases (Fig. 10(f)), and the deposition efficiency decreases slightly (Fig. 11(f)).

4.7. *Effects of the rotational speed of the target*

The effects of the rotational speed of the boule were investigated. Calculations were carried out for speeds of 60, 120 and 300 r.p.m. The overall flow and temperature contours are slightly shifted in the direction of rotation; the stagnation point is at 3 , the separation points are at 135 and −130 for $N = 300$ r.p.m. However, the maximum deposition rate occurs at 15° (Fig. 14(b)) mainly due to the changes in the concentration distribution. Rotation only slightly reduces the efficiency (Fig. 15). These effects will be more important when the radius of the target is large and the gas speed is small.

5. CONCLUSIONS

The flow, heat transfer, particle deposition and efficiency in the OVD process have been studied. The following conclusions are drawn.

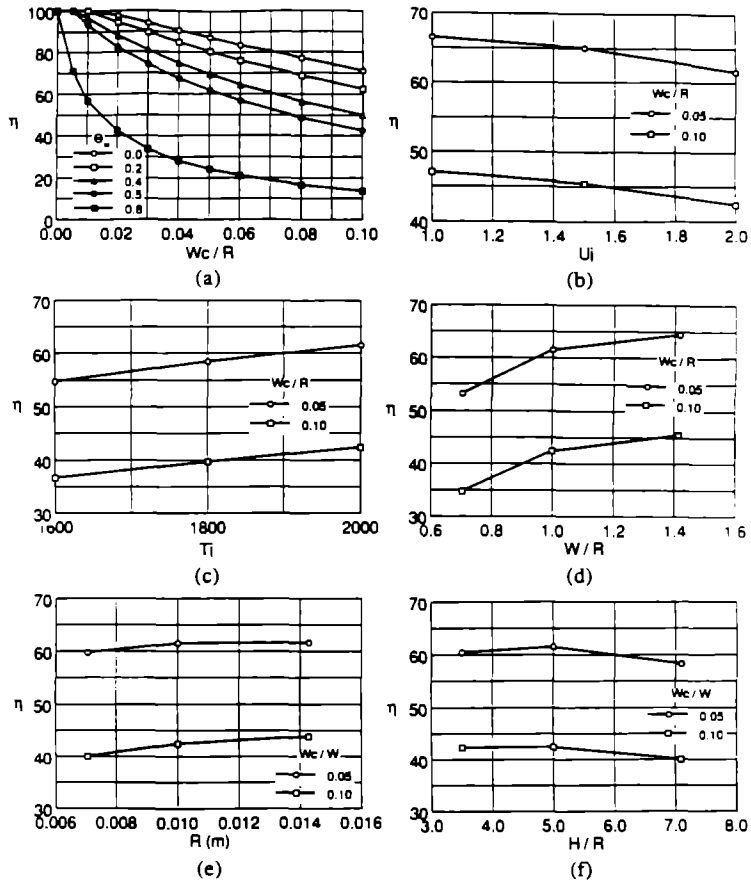

FIG. 11. Variations of the deposition efficiency with variables: (a) Θ_w and W_c/R; (b) U_i; (c) T_i; (d) W/R; (e) R; (f) H/R.

(1) Buoyancy accelerates the flow towards the target and significantly increases the skin-friction and heat transfer. The flow cools by heat transfer to the surroundings and to the target. The interaction of the jet-like torch flow with the target results in a flow and heat transfer that are quite different from that for uniform flow.

(2) The increase of the concentration prior to the target increases the particle deposition rate. The concentration and the deposition rate decrease from the stagnation point to downstream locations and become very small in the recirculation region. Buoyancy causes an increase in the deposition efficiency.

(3) The average Nusselt number and efficiency

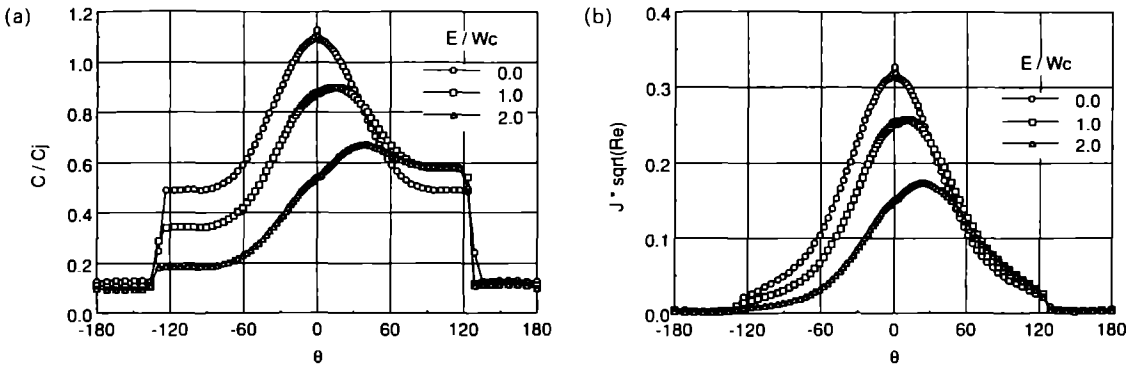

FIG. 12. (a) Variations of particle concentration on the surface with eccentricity of the torch. (b) Variations of deposition rate coefficiency on the surface with eccentricity of the torch.

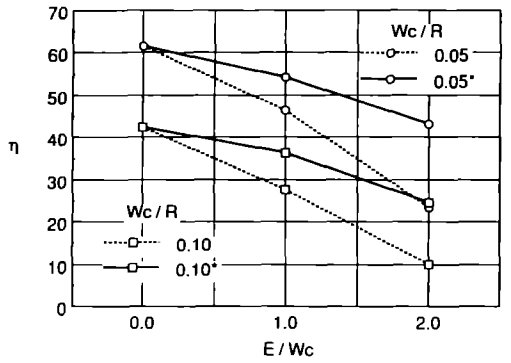

FIG. 13. Variations of the deposition efficiency with eccentricity of the torch; { }* denotes the values when only the particle jet is misaligned.

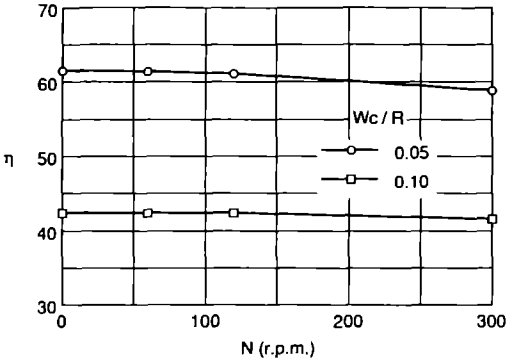

FIG. 15. Variations of the deposition efficiency with rotational speed of the target.

increase as the surface temperature becomes cold. For a hot target, the Nusselt number becomes negative over the leeward side and a particle-free layer is formed. For a cold target the deposition coefficient increases especially near the stagnation point.

(4) As the particle jet becomes thin relative to the target and the gas jet, the concentration and the deposition rate rapidly decrease from the stagnation point to downstream locations. The deposition efficiency increases.

(5) Misalignment of the torch with respect to the target destroys the symmetry of the particle jet and reduces the maximum concentration. The deposition efficiency is significantly reduced by misalignment.

(6) Increasing the speed of the jet increases the average Nusselt number, but reduces the efficiency. A higher jet temperature results in smaller Nusselt numbers and a higher efficiency.

(7) As the target grows, the efficiency is slightly increased.

(8) As the distance between the torch and the target becomes greater, the average Nusselt number decreases, and the deposition efficiency decreases very slightly.

(9) The rotational speed of the boule slightly reduces the efficiency primarily due to the changes in the concentration distribution.

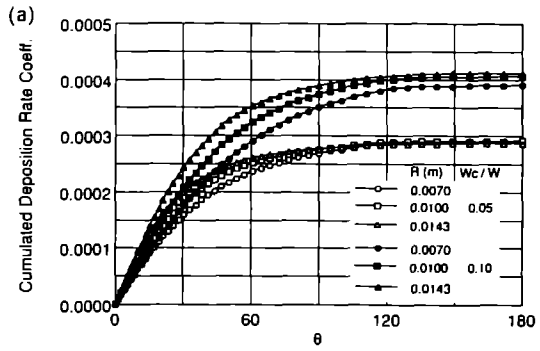

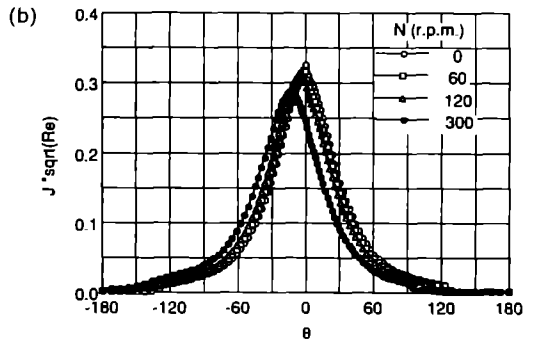

FIG. 14. (a) Variations of cumulated deposition coefficients with target radius. (b) Variations of deposition coefficiency on the surface with rotational speed of the target.

Acknowledgements—Support from the National Science Foundation, the San Diego Supercomputer Center and the Computer Center of the University of California at Berkeley is gratefully acknowledged. The authors acknowledge many fruitful conversations with J. Hwang and J. W. Daily who are carrying out experiments to enhance and control deposition rates in collaboration with our work. The authors are indebted to J. A. C. Humphrey for the use of his numerical code for non-orthogonal coordinates.

REFERENCES

1. A. J. Morrow, A. Sarkar and P. C. Schultz, Outside vapor deposition. In *Optical Fiber Communications* (Edited by T. Li), Vol. 1, pp. 65–96. Academic Press, New York (1985).
2. J. R. Bautista, E. Potkay and D. L. Scatton, Particle size measurement in optical waveguide manufacturing torches using dynamic light scattering, *Mat. Res. Soc., Symp. Proc.* **117**, 151–156 (1988).
3. G. M. Homsy, F. T. Geyling and K. L. Walker, Blasius series for thermophoretic deposition of small particles, *J. Colloid Interface Sci.* **83**(2), 495–501 (1981).
4. G. K. Batchelor and C. Shen, Thermophoretic deposition of particles in gas flowing over cold surfaces, *J. Colloid Interface Sci.* **107**(1), 21–37 (1985).
5. S. A. Gokoglu and D. E. Rosner, Viscous dissipation effects on thermophoretically-augmented aerosol par-

ticle transport across laminar boundary layers, *Int. J. Heat Fluid Flow* **6**, 293–297 (1985).
6. S. A. Gokoglu and D. E. Rosner, Thermophoretically augmented mass transfer rates to solid walls across laminar boundary layers, *AIAA J.* **24**, 172–179 (1986).
7. V. K. Garg and S. Jayaraj, Thermophoretic deposition over a cylinder, *Int. J. Engng Fluid Mech.* **3**(2), 175–196 (1990).
8. V. K. Garg and S. Jayaraj, Thermophoretic deposition in crossflow over a cylinder, *J. Thermophys.* **4**(1), 115–116 (1990).
9. M. K. Alam, G. Graham, V. Janakiraman and J. Greaves, Numerical analysis of thermophoretic transport in the OVD process, *ASME Numerical Heat Transfer*, HTD-Vol. 130, pp. 67–72 (1990).
10. J. R. Bautista, K. L. Walker and R. M. Atkins, Modeling of heat transfer and mass transfer in the manufacture of optical waveguides, *A.I.Ch.E. Natn. Meeting*, Washington, DC (1988).
11. G. M. Graham and M. K. Alam, Experimental study of the outside vapor deposition process, *Aerosol Sci. Technol.* **15**, 69–75 (1992).
12. J. Hwang and J. W. Daily, A study of particle charging for electric field enhanced deposition, *Aerosol Sci. Technol.* **16**, 113–125 (1992).
13. J. Hwang and J. W. Daily, Temperature and electric field measurements for particle thermophoresis and electrophoresis in an optical waveguide flame, submitted for publication.
14. J. Hwang and J. W. Daily, Electric field enhanced deposition in flame-synthesized and materials manufacturing, submitted for publication.
15. S. H. Kang and R. Greif, Flow and heat transfer to a circular cylinder with a hot impinging air jet, *Int. J. Heat Mass Transfer* **35**, 2175–2184 (1992).
16. J. F. Thompson, Z. A. Warsi and C. W. Mastin, *Numerical Grid Generation, Foundations and Applications*. North-Holland, New York (1985).
17. M. J. Schuh, Numerical prediction of fluid and particle motions in flows past tubes, Ph.D. Thesis, University of California, Berkeley (1987).
18. M. J. Schuh, C. A. Schuler and J. A. C. Humphrey, Numerical calculation of particle-laden gas flows past tubes, *A.I.Ch.E. Jl* **35**(3), 466–480 (1989).
19. L. Talbot, R. K. Cheng, R. W. Schefer and D. R. Willis, Thermophoresis of particles in a heated boundary layer, *J. Fluid Mech.* **101**, 737–758 (1980).
20. K. L. Walker, F. T. Geyling and S. R. Nagel, Thermophoretic deposition of small particles in the modified chemical vapor deposition (MCVD) process, *J. Am. Ceram. Soc.* **63**, 552–558 (1980).
21. S. V. Patankar, *Numerical Heat Transfer and Fluid Flow*. Hemisphere, New York (1980).
22. G. E. Schneider and M. Zedan, A modified strongly implicit procedure for the numerical solution of field problems, *Numer. Heat Transfer* **4**, 1–19 (1981).
23. T. Cebeci and P. Bradshaw, *Physical and Computational Aspects of Convective Heat Transfer*. Springer, Berlin (1984).
24. M. Epstein, G. M. Hauser and R. E. Henry, Thermophoretic deposition of particles in natural convection flow from a vertical plate, *J. Heat Transfer* **107**, 272–276 (1985).

APPENDIX A. EVALUATION OF CONCENTRATION ON THE SURFACE FROM THE NORMAL GRADIENT OF TEMPERATURE

If the streamwise conduction and thermophoretic particle transport terms are neglected in the energy and the concentration equations in the surface fitted orthogonal coordinates (s, n), the following boundary layer equations are obtained:

$$c_p\left[\frac{\partial(\rho u T)}{\partial s}+\frac{\partial(\rho v T)}{\partial n}\right]=\frac{\partial}{\partial n}\left(k\frac{\partial T}{\partial n}\right) \tag{A1}$$

$$\frac{\partial(uC)}{\partial s}+\frac{\partial(vC)}{\partial n}=\frac{\partial}{\partial n}\left(K\frac{vC}{T}\frac{\partial T}{\partial n}\right). \tag{A2}$$

The density, conductivity and dynamic viscosity are given by

$$\frac{\rho}{\rho_a}=\left(\frac{T}{T_a}\right)^{-1},\quad \frac{k}{k_a}=\left(\frac{T}{T_a}\right)^{p},\quad \frac{\mu}{\mu_a}=\left(\frac{T}{T_a}\right)^{q}. \tag{A3}$$

The right-hand side of equation (A1) can be written as

$$kT''+\frac{\mathrm{d}k}{\mathrm{d}T}(T')^2=k\left[T''+p\frac{(T')^2}{T}\right] \tag{A4}$$

where $\{\quad\}'$ denotes the partial derivative with respect to the normal coordinate n. The variation of conductivity plays the role of a heat source in the energy equation. On the surface, the velocity is zero and equations (A1) and (A4) yield

$$T''_w=-p\frac{(T'_w)^2}{T_w}. \tag{A5}$$

In the same way, the right-hand side of equation (A2) can be written as

$$\left(\frac{KvC}{T}T'\right)'=Kv'\frac{CT'}{T}+Kv\frac{C'T'}{T}-KvC\frac{(T')^2}{T^2}+\frac{KvC}{T}T''$$

$$=K(1+q)v\frac{C(T')^2}{T^2}+Kv\frac{C'T'}{T}-KvC\frac{(T')^2}{T^2}-\frac{Kvp(T')^2}{T^2}C. \tag{A6}$$

I II III IV

The terms on the right-hand side of equation (A6) represent:

I—effect of viscosity variation on the thermophoretic velocity;
II—variation of the concentration;
III—effect of temperature variation on the thermophoretic velocity; and
IV—indirect effect of conductivity variation on the thermophoretic velocity.

On the surface, the velocity is zero and equations (A2) and (A6) yield

$$\frac{C'_w}{C_w}=\{1.0+p-(1+q)\}\frac{T'_w}{T_w}=(p-q)\frac{T'_w}{T_w}. \tag{A7}$$

When T'_w and T_w are known, the value of C_w can be obtained by utilizing equation (A7) and the value of the concentration at an interior point in a finite difference formulation. For air, $p=0.785$ and $q=0.673$ and for helium $p=0.618$ and $q=0.646$ when the data (Cebeci and Bradshaw [23]) are used. The terms in the brackets of equation (A7), $\{1.0, p,$ and $q+1\}$ are the effects of the temperature distribution, the variation of the conductivity k, and the variation of the kinetic viscosity μ/ρ, respectively. Note for $p=q$ the normal gradient of the concentration at the wall is zero. Epstein *et al.* [24] considered the case of constant properties and obtained $C'_w/C_w=T'_w/T_w$.

APPENDIX B. CORRELATION BETWEEN VARIATION OF TEMPERATURE AND CONCENTRATION ALONG THE CENTER LINE OF THE TORCH

The relation between temperature and concentration variations along the center line of the jet is obtained. The concentration equation (6) is written by

$$u\frac{\partial C}{\partial x}+v\frac{\partial C}{\partial y}=-C\left(\frac{\partial u}{\partial x}+\frac{\partial v}{\partial y}\right)+\frac{\partial}{\partial x}\left(\frac{KvC}{T}\frac{\partial T}{\partial x}\right)$$
$$+\frac{\partial}{\partial y}\left(\frac{KvC}{T}\frac{\partial T}{\partial y}\right)=\frac{C}{\rho}\left(u\frac{\partial \rho}{\partial x}+v\frac{\partial \rho}{\partial y}\right)$$
$$+\frac{\partial}{\partial x}\left(\frac{KvC}{T}\frac{\partial T}{\partial x}\right)+\frac{\partial}{\partial y}\left(\frac{KvC}{T}\frac{\partial T}{\partial y}\right). \quad \text{(B1)}$$

Since ρ and C are symmetric with respect to the center line of the jet, i.e. at $y=0$, equation (B1) becomes

$$\frac{1}{C}\frac{\partial C}{\partial x}=\frac{1}{\rho}\frac{\partial \rho}{\partial x}+\frac{1}{uC}\left[\frac{\partial}{\partial x}\left(\frac{KvC}{T}\frac{\partial T}{\partial x}\right)+\frac{\partial}{\partial y}\left(\frac{KvC}{T}\frac{\partial T}{\partial y}\right)\right]$$
$$=-\frac{1}{T}\frac{\partial T}{\partial x}+\frac{1}{uC}\left[\frac{\partial}{\partial x}\left(\frac{KvC}{T}\frac{\partial T}{\partial x}\right)+\frac{\partial}{\partial y}\left(\frac{KvC}{T}\frac{\partial T}{\partial y}\right)\right]. \quad \text{(B2)}$$

The variation of temperature along the center line can be obtained from equation (4):

$$\frac{\partial T}{\partial x}=\frac{k}{\rho c_p u}\left[\left(\frac{\partial^2 T}{\partial x^2}+\frac{\partial^2 T}{\partial y^2}\right)+\frac{p}{T}\left(\frac{\partial T}{\partial x}\right)^2\right]. \quad \text{(B3)}$$

This can be rewritten as

$$\frac{\partial^2 T}{\partial x^2}+\frac{\partial^2 T}{\partial y^2}=\frac{\rho c_p u}{k}\frac{\partial T}{\partial x}-\frac{p}{T}\left(\frac{\partial T}{\partial x}\right)^2. \quad \text{(B4)}$$

The thermophoretic diffusion term along the center line can be written as

$$\frac{\partial}{\partial x}\left(\frac{KvC}{T}\frac{\partial T}{\partial x}\right)+\frac{\partial}{\partial y}\left(\frac{KvC}{T}\frac{\partial T}{\partial y}\right)$$
$$=\frac{KvC}{T}\left[\frac{\partial^2 T}{\partial x^2}+\frac{\partial^2 T}{\partial x^2}+\frac{q}{T}\left(\frac{\partial T}{\partial x}\right)^2+\frac{1}{C}\frac{\partial C}{\partial x}\frac{\partial T}{\partial x}\right]. \quad \text{(B5)}$$

From equations (B2) and (B5) the following relation is obtained:

$$\frac{1}{C}\frac{dC}{dx}=(-1.0+K\cdot Pr)\frac{1}{T}\frac{dT}{dx}$$
$$+(q-p)\frac{Kv}{u}\left(\frac{1}{T}\frac{dT}{dx}\right)^2+\frac{Kv}{u}\left(\frac{1}{C}\frac{dC}{dx}\right)\left(\frac{1}{T}\frac{dT}{dx}\right)$$
$$=(-1.0+K\cdot Pr)\frac{1}{T}\frac{dT}{dx}+O\left[\left(\frac{1}{T}\frac{dT}{dx}\right)^2\right]. \quad \text{(B6)}$$

Neglecting the second-order term in equation (B6) and integrating with respect to x yields

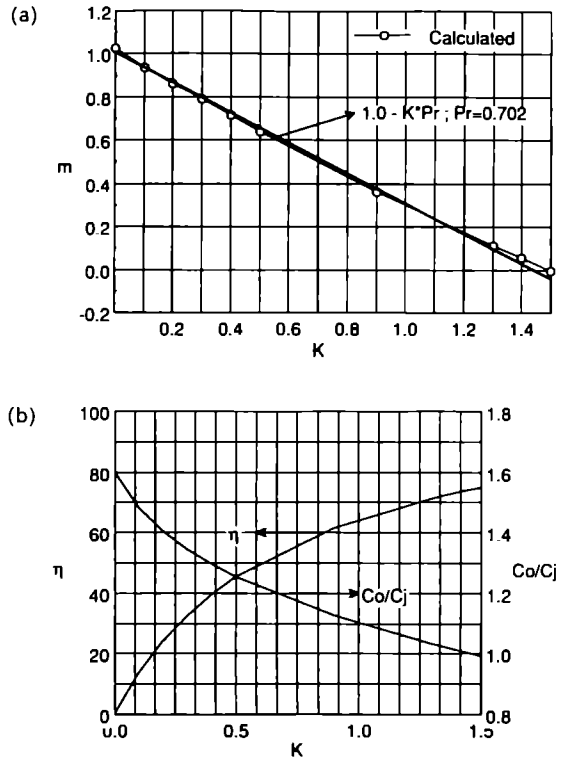

FIG. B1. (a) Calculated coefficients of the temperature and concentration correlation. (b) Variations of the deposition efficiency and particle concentration at the stagnation point.

$$\frac{C(x,0)}{C_j}=\left[\frac{\Theta(x,0)+\Theta^*}{1.0+\Theta^*}\right]^{-(1.0-K\cdot Pr)} \quad \text{(B7)}$$

where $\Theta=(T-T_a)/(T_j-T_a)$ and $\Theta^*=T_a/(T_j-T_a)$. Calculations were carried out for the standard values of the parameters with different values of K. The calculated coefficients m (equation (13)) are in good agreement with $(1.0-K^*Pr)$ as shown in Fig. B1(a). For $K=1.5$, i.e. $m=0.0$, the particle concentration is nearly constant along the center line. The thermophoretic velocity on the surface is proportional to K and the concentration of particles is reduced for large K. The variations of the deposition efficiency and the concentration at the stagnation point with respect to K are presented in Fig. B1(b). It is seen that the thermophoretic coefficient K can have a significant effect on the deposition efficiency and the concentration at the stagnation point.